Journal of Advanced Ceramics
2022, **11**(12): 1956–1975
https://doi.org/10.1007/s40145-022-0659-2
ISSN 2226-4108
CN 10-1154/TQ

Research Article

Elucidating the role of preferential oxidation during ablation: Insights on the design and optimization of multicomponent ultra-high temperature ceramics

Ziming YE, Yi ZENG*, Xiang XIONG*, Qingbo WEN, Huilin LUN

State Key Laboratory of Powder Metallurgy, *Central South University*, *Changsha 410083*, *China*

Received: April 28, 2022; Revised: September 2, 2022; Accepted: September 6, 2022

Abstract: Multicomponent ultra-high temperature ceramics (UHTCs) are promising candidates for thermal protection materials (TPMs) used in aerospace field. However, finding out desirable compositions from an enormous number of possible compositions remains challenging. Here, through elucidating the role of preferential oxidation in ablation behavior of multicomponent UHTCs via the thermodynamic analysis and experimental verification, the correlation between the composition and ablation performance of multicomponent UHTCs was revealed from the aspect of thermodynamics. We found that the metal components in UHTCs can be thermodynamically divided into preferentially oxidized component (denoted as M_P), which builds up a skeleton in oxide layer, and laggingly oxidized component (denoted as M_L), which fills the oxide skeleton. Meanwhile, a thermodynamically driven gradient in the concentration of M_P and M_L forms in the oxide layer. Based on these findings, a strategy for pre-evaluating the ablation performance of multicomponent UHTCs was developed, which provides a preliminary basis for the composition design of multicomponent UHTCs.

Keywords: multicomponent ceramics; ultra-high temperature ceramics (UHTCs); preferential oxidation; oxidation behavior; ablation resistance

1 Introduction

Newly developed single-phase multicomponent ceramics (including high-entropy ceramics) is a class of solid solutions containing at least three metal elements, which are expanding the scope of discovering and implementation of better-performance thermal protection materials (TPMs) [1–7]. These novel multicomponent ceramics exhibit improved mechanical and thermal stability [8–10], diminished thermal conductivity [11–13], and higher hardness [2,14] compared with their original monocarbides, diborides, etc. In particular, researchers [1,4,15–22] have confirmed the remarkably enhanced oxidation resistance of multicomponent ceramics recently. This new paradigm in ultra-high temperature ceramics (UHTCs) will hopefully meet the increasing demand for high-temperature capability in the aerospace field. However, due to the absence of effective and facile guidance for finding out the desirable combination or ratio of components, the design and optimization of multicomponent UHTCs usually necessitate extensive experimental work towards a large number of possible compositions, which makes it expensive and time consuming. Hence, a systematic understanding of the

* Corresponding authors.
E-mail: Y. Zeng, zengyi001@csu.edu.cn;
X. Xiong, xiongx@csu.edu.cn

correlation between the components, oxidation behavior, and final ablation performance is highly demanded.

The superior oxidation resistance of multicomponent UHTCs is closely correlated with their compositional and structural evolution during oxidation. These unique oxidation behaviors enhance the integral protection performance of multicomponent UHTCs against oxidizing environments [3,5,15,17,18]. For instance, the establishment of a "stable Hf/Zr-rich skeleton filled with Ti-rich melts" structure in protective oxide scale and the formation of multicomponent carbonaceous oxide interlayer which acts as a primary oxygen diffusion barrier in carbide case, are of great benefit to oxidation resistance [17,18,23]. More importantly, these favorable oxidation behaviors exhibit a strong compositional-dependence that is significantly associated with the tendency of preferential oxidation of thermodynamically favored components [3,24,25]. However, the specific role of preferential oxidation in the compositional and structural evolution of multicomponent ceramics as well as their correlation with oxidation performance remain unclear. Meanwhile, the tendency of preferential oxidation is considered to be temperature-dependent [3,24], yet the impacts of temperature on preferential oxidation are unexplored.

In this work, experimental investigation in conjunction with thermodynamic analysis was conducted in order to elucidate the role of preferential oxidation in the ablation behavior of multicomponent UHTCs. Importantly, the correlation between the composition and ablation performance of multicomponent ceramics was revealed based on thermodynamic elucidation. In addition, new insights into the temperature-dependent nature of the preferential oxidation were provided. Moreover, a strategy for pre-evaluating the ablation performance of multicomponent UHTCs was proposed, and then experimentally validated. The aim of this work is to provide a preliminary basis for the composition design of multicomponent UHTCs.

2 Materials and method

2. 1 Material preparation

In this work, for the purpose of improving the thermal-shock resistance and decreasing the risk of cracking during the ablation test, the designed multicomponent carbides were incorporated into porous C/C composite (density = 1.00 g·cm^{-3}) via a reactive melting infiltration (RMI) process in argon (Ar) at 2200 ℃ for 30 min. In this process, the C/C samples were placed onto Zr powder and three mixed powders with the following compositions: (1) 50 at% Hf–30 at% Zr–20 at% Ti, (2) 50 at% Hf–30 at% Zr–10 at% Ti–10 at% Ta, and (3) 50 at% Hf–30 at% Zr–10 at% Ti–10 at% Nb. During the RMI process, the solution of molten metals was infiltrated into the porous C/C composites by capillary forces and reacted with the carbon, forming the carbide/carbon composites. In the composites, multicomponent carbides were formed on the C/C reinforcements *in-situ*, while some carbides were allowed to infiltrate into the reinforcements.

2. 2 Ablation test

The ablation test was performed by a plasma torch device. The distance between the gun tip and the specimen was 55 mm. The specimen, with the dimension of Ø30 mm × 10 mm, was fixed in a water-cooled copper sample holder and exposed to flame for 120 s. The fluxes of Ar and H_2 were set as 2000 and 180 L·h^{-1}, respectively. The working current and voltage were 699 A and 64 V, respectively. The heat flux of the plasma torch was measured to be 6.73 MW·m^{-2} by a heat flux sensor (GD-B3-12M, Beijing Eastsummit Tech. Inc.). Whilst the temperatures reached 2540–2730 K, which was measured by an optical pyrometer, and the optical pyrometer was aimed at the ablation center of the sample. The schematic illustration is shown in Fig. S1 in the Electronic Supplementary Material (ESM). The extreme oxidizing scenario at 3273.15 K was established by oxyacetylene ablation test according to Ref. [4]. The linear ablation rate (LAR) and mass ablation rate (MAR) can be calculated by Eqs. (1) and (2), respectively:

$$\mathrm{LAR} = \frac{d_\mathrm{i} - d_\mathrm{f}}{t} \tag{1}$$

$$\mathrm{MAR} = \frac{m_\mathrm{i} - m_\mathrm{f}}{t} \tag{2}$$

where d_i (μm) and d_f (μm) are the initial and final thicknesses measured at the center of the sample, respectively; m_i (mg) and m_f (mg) are the initial and final masses of the sample, respectively; and t (s) is the testing time.

2. 3 Characterization

The phase compositions were analyzed by using a rotating-target X-ray diffractometer (D/max 2550vb+

18 kW, Rigaku) at a scanning rate of 2 (°)·min^{-1}. The morphology was characterized under a scanning electron microscope (SEM; MIRA4 LMH, TESCAN) combined with an energy dispersive spectrometer (Ultam-Max-50). The high-resolution transmission electron microscopy (HRTEM) images and high-angle annular dark field scanning transmission electron microscopy (HAADF-STEM) images were obtained by an electron microscope (F200x, Talos) equipped with an energy dispersive spectroscometer. The TEM samples were prepared by a focused ion beam (FIB; Helios Nanolab 600i, FEI) using the *in-situ* lift-out technique on cross-sections of the samples. The bulk density and open porosity were measured according to the Archimedes method. The 3D surface profile was obtained with a digital microscope (VHX-6000, KEYENCE).

3 Results

3. 1 Compositional and structural evolution of multicomponent UHTCs during ablation

In order to reveal the ablation behavior of the multicomponent UHTCs that resulted from preferential oxidation, the composition and structure of a typical multicomponent carbide (i.e., $Hf_{0.5}Zr_{0.3}Ti_{0.2}C$) during ablation were investigated in multiscale. The as-fabricated carbide possesses a density of 8.65 g·cm^{-3}, and the relative density is 93% [26]. The relative dense morphology is confirmed by the SEM image (Fig. 1(a)), while the microscale (Fig. 1(d)) and nanoscale (Fig. 1(e)) energy dispersive spectroscopy (EDS) elemental mappings, which were obtained from the SEM–EDS

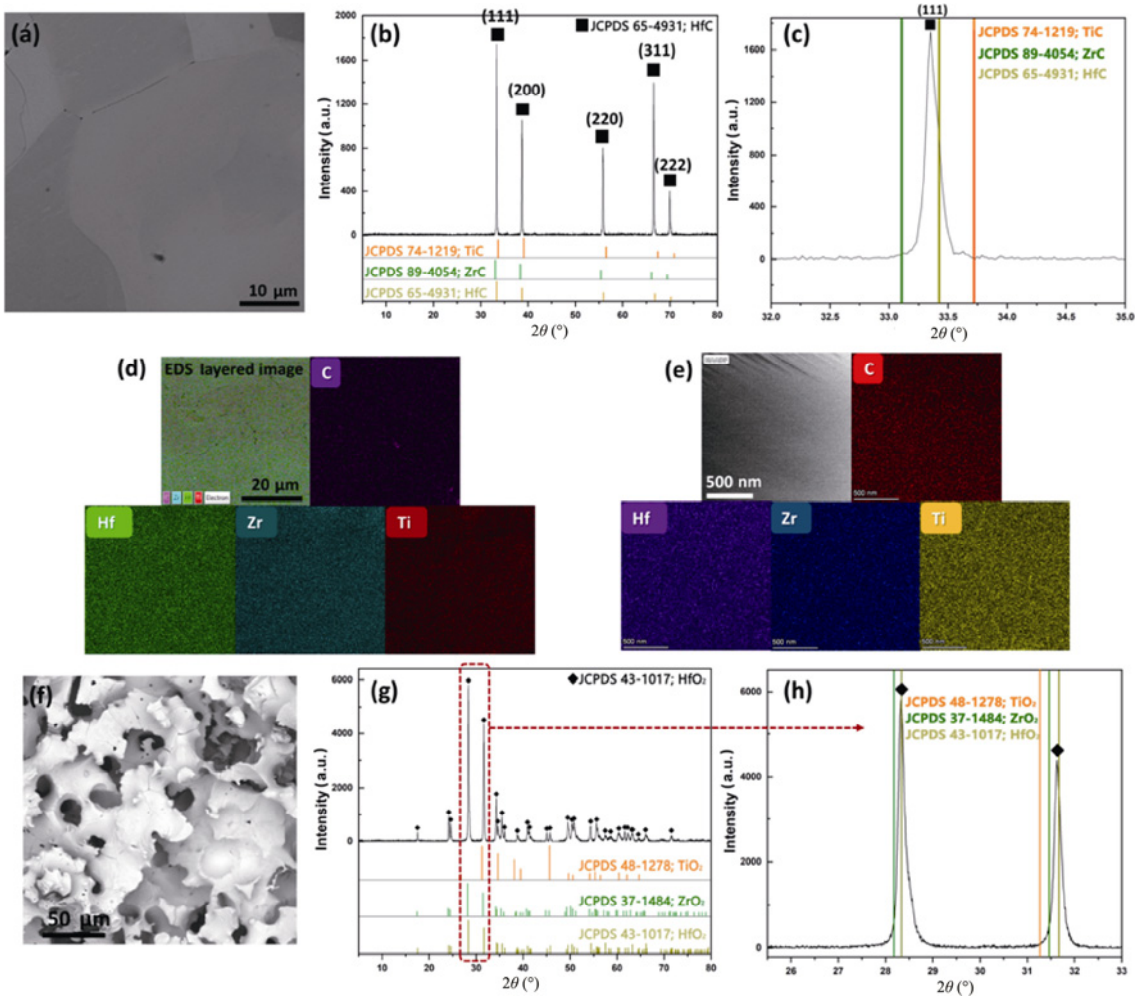

Fig. 1 (a) SEM image of polished cross-section of bulk $Hf_{0.5}Zr_{0.3}Ti_{0.2}C$. (b) XRD patterns of the bulk carbide. (c) Magnified pattern at (111) and peak positions of pristine HfC (yellow line), ZrC (green line), and TiC (orange line). (d, e) Microscale and nanoscale EDS elemental mappings of $Hf_{0.5}Zr_{0.3}Ti_{0.2}C$ by the SEM–EDS and STEM–EDS, respectively. (f) Microstructure of central-ablated surface. (g) XRD patterns of the ablated surface. (h) Magnified patterns with peak positions at (−111) and (111) and peak positions of pristine HfO_2 (yellow line), ZrO_2 (green line), and TiO_2 (orange line).

and STEM–EDS, respectively, prove the uniform distribution of metal elements. As shown in the X-ray diffraction (XRD) patterns (Figs. 1(b) and 1(c)), the major peaks of the carbide can be indexed to the face-centered cubic (fcc) HfC (JCPDS 65-4931). In comparison to pristine HfC, the multicomponent carbide phase exhibits a small shift of the XRD peaks to a lower angle, and its peak positions are between pristine ZrC and TiC, as shown in Fig. 1(c). Given the fact that the radius of a Zr atom (0.160 nm) is close to and slightly larger than those of a Hf atom (0.158 nm) and a Ti atom (0.146 nm), respectively, it can be inferred that during the RMI, HfC-dissolved Zr and Ti atoms form the solid solution phase of $Hf_{0.5}Zr_{0.3}Ti_{0.2}C$, thus resulting in this small shift to a lower angle [18]. And the formation of similar solid solution phases is also reported in Ref. [19]. The extreme oxidizing scenario at ca. 2620 K was established by a plasma ablation test. After ablation, it is observed that oxides partially melted in the central surface (Fig. 1(f)). A set of peaks indexed to monoclinic HfO_2 (JCPDS 43-1017) with a small shift to a lower angle is detected in the XRD patterns (Figs. 1(g) and 1(h)), which is similar to those indexed to $Hf_{0.5}Zr_{0.3}Ti_{0.2}C$. This also suggests that multicomponent oxide solid solutions of Hf–Zr–Ti–O formed.

As shown in the SEM image of the cross-section of the central-ablated region (Fig. 2(a)), an oxygen-and-carbon-containing interlayer (i.e., the carbonaceous oxide interlayer [18]) is observed between the oxide layer and the bulk material via the EDS line analysis (Figs. S2(a) and S2(d) in the ESM). Thus, the $Hf_{0.5}Zr_{0.3}Ti_{0.2}C$ demonstrates a typical oxidation behavior of multicomponent carbide [17,18]. Notably, a unique

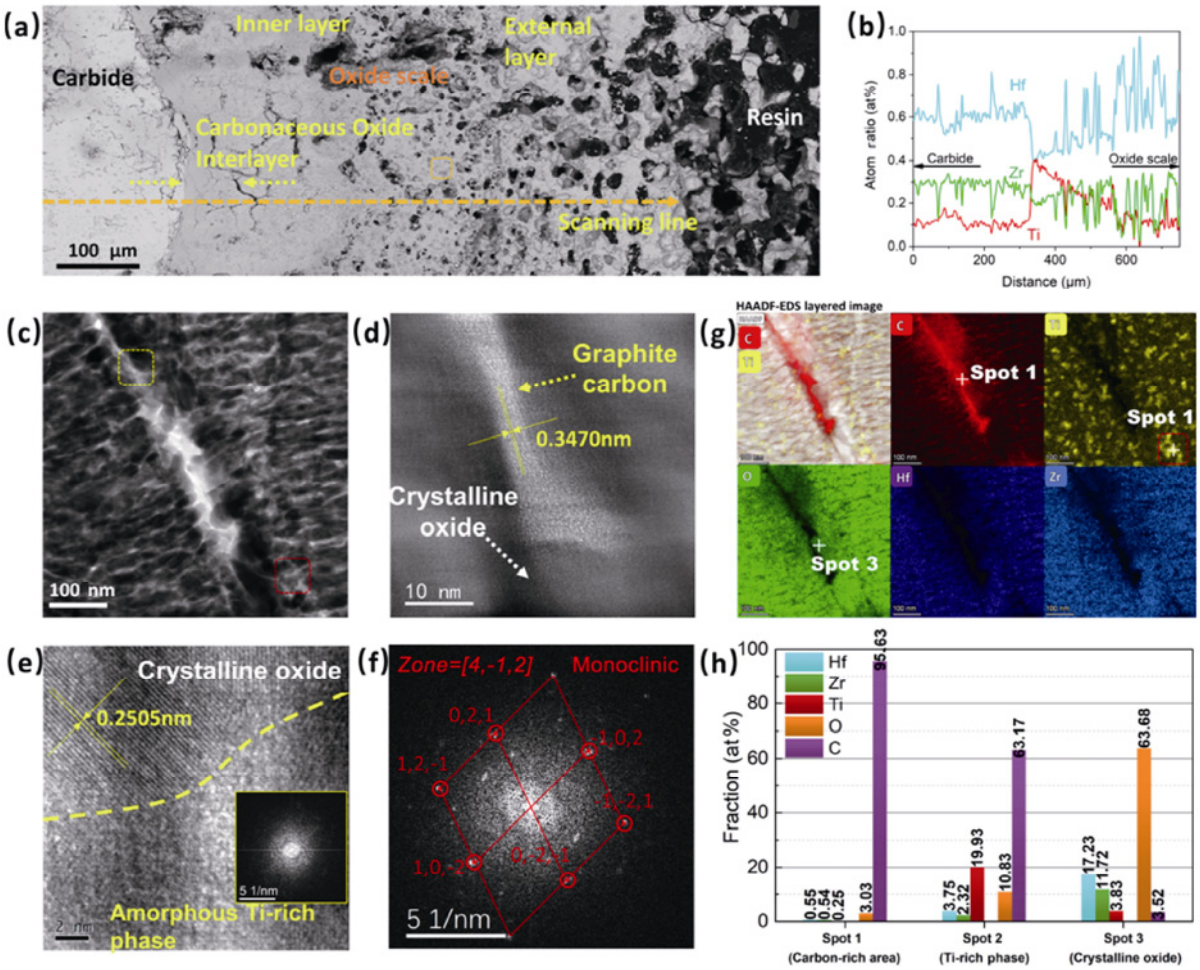

Fig. 2 (a) SEM image of cross-section of the central region ablated at 2620 K. (b) Cross-section EDS line profiles reveal metal element distributions. (c) TEM image of the oxidized region at the interlayer. (d) HRTEM image of graphite carbon at grain boundaries (i.e., the yellow and red boxes in (c)). (e) HRTEM image of the red box in (c); the inset is the fast Fourier transform (FFT) patterns. (f) FFT pattern of the crystalline oxides. (g) HAADF-EDS-layered image and corresponding elemental mappings (C, O, Hf, Zr, and Ti). (h) EDS point analysis at the three spots in (g).

concentration gradient of metal elements appears along the depth direction of the ablated sample. The EDS line profiles (Fig. 2(b)) reveal an incremental concentration of Ti from the surface to the inner layer of the oxide scale, whereas the concentrations of Hf and Zr significantly decrease. As predicted, Hf and Zr will be preferentially oxidized over Ti in this system [24]. It indicates that at the macro level, the preferential oxidation of Hf and Zr in Hf–Zr–Ti–C system will result in the compositional evolution of gradual enrichment of Ti with the depth of the oxide scale.

In order to further reveal the structural evolution of multicomponent UHTCs during ablation, a thin slice was lifted out from the carbonaceous oxide interlayer (the exact position is shown in Fig. S3(a) in the ESM) via the FIB milling process, and then analyzed by the TEM. As illustrated in Fig. 2(c), this oxidation interface region mainly consists of a grain skeleton, which can be indexed to monoclinic HfO_2 (JCPDS 43-1017, Figs. 2(d) and 2(f)). Besides, the (−102) interplanar spacing of the oxide grain is ~0.2505 nm, which is close to that of HfO_2 (0.2486 nm for (−102), JCPDS 43-1017). The corresponding STEM–EDS analysis (Spot 3 in Figs. 2(g) and 2(h)) confirms that these oxides are mostly rich in Hf and Zr. Moreover, graphite-like carbon with a typical layered structure (Fig. 2(d), a magnified view of the yellow box in Fig. 2(c)) is observed along the grain boundaries. While the (002) interplanar spacing of this graphite-like carbon is measured to be 0.3470 nm, and this value is close to that of the graphite (0.3395 nm, JCPDS 75-1621). Combining the STEM–EDS analysis (Spot 1 in Figs. 2(g) and 2(h)) with the elemental mapping of carbon (Fig. 2(g)), the grain boundaries and micro-voids are demonstrated to be carbon-rich areas [18]. Meanwhile, it can be inferred from the HRTEM image (Fig. 2(e)), a magnified view of the red box in Fig. 2(c)) that some amorphous phases also gathered at the grain boundaries and micro-voids, while the elemental mapping of Ti and EDS results of Spot 2 (Figs. 2(g) and 2(h)) prove that these amorphous phases are Ti-rich phases and probably contain part of carbon.

Generally, as indicated by the TEM analysis, the partially oxidized carbon-enriched areas correspond with the enrichment of Ti. In contrast, the oxides are mostly rich in Hf and Zr. This result is in good agreement with the prediction that Hf and Zr would be preferentially oxidized over Ti. Moreover, further investigations reveal that the inner oxide layer and ablated surface also possess apparent structure of Hf/Zr rich oxide grain skeleton infilled with Ti-rich oxide. As the STEM micrograph (Fig. 3(a)) and HRTEM observation (Fig. 3(b)) of the inner oxide layer depict, the structure of grain skeleton is sealed by amorphous phases. The composition analyses in Table 1 confirm the relative enrichment of Ti in these likely-amorphous phases, whereas the crystalline oxides are rich in Hf and Zr. In addition, the areas of amorphous phase in grain boundaries appear to be darker than the crystalline part in the SEM micrograph of the inner oxide layer (Fig. 3(c)). As shown in Fig. 3(d) and Table 1, significant Hf–Zr-enrichment occurs within the surface oxides, further confirming the preferential oxidation of Hf and Zr. Interestingly, the likely-amorphous Ti-rich phase appears again at the Hf/Zr-rich oxide grain boundary (indicated by the yellow arrows in Fig. 3(d)). In addition, the formation of these oxide grain skeleton and amorphous phase is closely correlated with their melting points. It is observed from the HfO_2–TiO_2 [27] and ZrO_2–TiO_2 [28] phase diagrams that steeply rising the liquidus temperature appears near the region containing 20–30 mol% TiO_2. As the Ti content in a multicomponent system was designed to be 20 at%, it is inferred that the melting phase could be formed *in-situ* in the as-formed Ti-rich region due to its lower melting point while the Ti-deficient oxide particle with a higher melting point

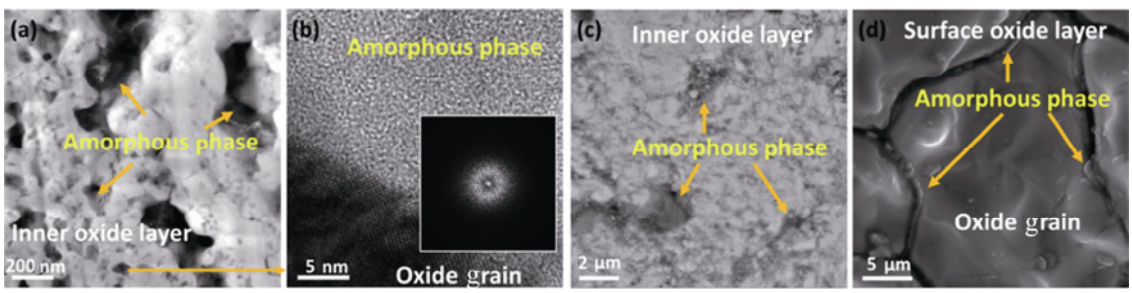

Fig. 3 (a) HAADF-STEM image of the inner oxide layer, (b) HRTEM image showing amorphous phase within (a) (the inset is the FFT pattern), (c) SEM image (backscattered electron) of the inner oxide layer (i.e., magnified view of the boxed region in Fig. 2(a)) showing amorphous phase and oxide grain, and (d) SEM image (secondary electron) of the top surface of oxide layer.

Table 1 Metal elemental ratios (at%) of amorphous phase and oxide grain within the interlayer, inner oxide layer, and ablated surface shown in Fig. 8; the result obtained by the SEM–EDS is averaged over three spots

Element		Hf	Zr	Ti
Interlayer (via the STEM–EDS analysis)	Amorphous phase	31.02	17.12	51.85
	Oxide grain	52.56	35.75	11.68
Inner oxide layer (via the SEM–EDS analysis)	Amorphous phase	43.74	23.34	32.88
	Oxide grain	58.50	29.91	11.59
Ablated surface (via the SEM–EDS analysis)	Amorphous phase	49.50	28.22	22.28
	Oxide grain	59.85	34.60	5.55

could remain solid and build up an adherent skeleton at the ablation temperature of 2620 K [18]. This can be supported by the STEM–EDS shown in Table 1, which indicates Ti contents of glassy oxide, and the crystalline oxide skeletons were determined to be 51.85% and 11.68%.

In summary, for multicomponent UHTCs, the preferentially oxidized component (denoted as M_P) would lead to the formation of M_P-rich oxide skeleton infilled with the oxides rich in laggingly oxidized component (denoted as M_L). Meanwhile, this preferential oxidation of M_P can also result in a gradual enrichment of M_L with the depth of the oxide scale.

4 Discussion

4. 1 Role of preferential oxidation on the compositional and structural evolution

In order to elucidate the specific role of preferential oxidation, thermodynamic analysis was conducted in the composition-dependent oxidation behavior of multicomponent carbide. Referring to the reported mechanistic models [29,30] and observations [18], the reaction interface of Hf–Zr–Ti–C is expected to possess a relatively low O_2 partial pressure ($p(O_2)$, approximately < 10^{-14}–10^{-10} Pa). In this context, the occurrence of preferential oxidation within the reaction interface is credited to the composition-dependent oxidation behavior under a unique local oxidation environment (i.e., the local $p(O_2)$). A thermodynamic approach was thus proposed to further interpret this unique oxidation behavior. Specifically, it is implemented by the analysis towards condensed phase equilibrium diagrams of MC+O_2 systems (M = Hf, Zr, Ti, Ta, Nb, etc.), which was calculated by the phase module of FactSage 7.3. In these diagrams, the abscissa and ordinate axes were set as $p(O_2)$ and temperature to describe the temperature–$p(O_2)$-gradient existing within the oxidation-affected zone. Importantly, the boundaries of stable range of carbides (i.e., edges of color blocks shown in Figs. 4(a)–4(c)), consisting of the equilibrium $p(O_2)$ values during oxidation under continuously varying temperature, are presented in these diagrams. Accordingly, comparative analysis of these diagrams enables the comparison of the thermodynamic stability of different components over an extended temperature range.

As shown in Fig. 4(d), the diagrams of component-HfC, -ZrC, and -TiC are combined into a compiled diagram. It can be observed that the equilibrium $p(O_2)$ of HfC and ZrC are significantly lower than that of TiC at temperatures below 2735 K (e.g., the ablation test at 2693.15 K mentioned above). Hence, under this circumstance, the aforementioned local $p(O_2)$ in the reaction interface would first reach the relative lower equilibrium $p(O_2)$ values of component-Hf and followed by that of component-Zr for multicomponent Hf–Zr–Ti–C (i.e., the yellow arrow and spot in Fig. 4(d)), while component-Ti will remain unoxidized at this moment because its equilibrium $p(O_2)$ is not yet reached. This implies that the components (e.g., Hf-species) with relatively lower equilibrium $p(O_2)$ will be preferentially oxidized during the oxidation process, resulting in the components (e.g., Ti-species) with relatively higher equilibrium $p(O_2)$ "lagging" other components (e.g., Hf-species) in the extent of oxidation. Through this thermodynamic diagram, the occurrence of the preferential oxidation is interpreted from the different equilibrium states of each component under a unique local oxidation environment.

Therefore, for a M_P–M_L-containing system, the structure evolution may start from the earlier nucleation of thermodynamically favored M_P-related oxide (e.g., HfO_2) according to the analysis, which shows that local $p(O_2)$ of reaction interface is too low to oxidize M_L (e.g., Ti-species) but high enough to oxidize M_P (e.g., Hf-species). Under this condition, nuclei of M_P-related oxide (e.g., HfO_2) would form among the

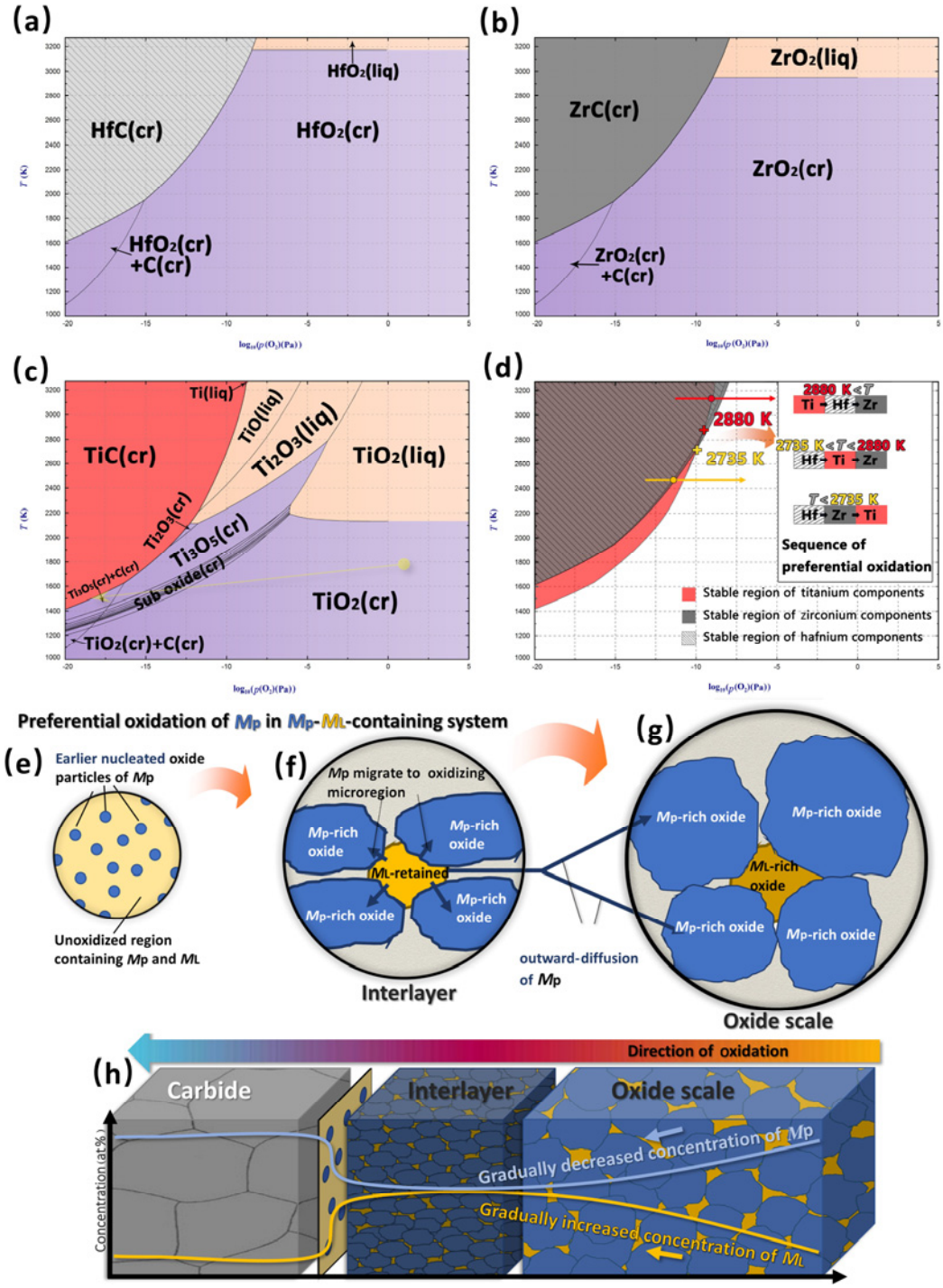

Fig. 4 Condensed phase equilibrium diagrams of (a) HfC, (b) ZrC, and (c) TiC; (d) compiled diagram of HfC–ZrC–TiC. (e–h) Schematic diagram depicting the role of preferential oxidation in the ablation behavior of multicomponent ceramics.

reaction interface. This inference can be substantiated by the HRTEM images and EDS analysis of the interlayer region adjacent to the carbide (i.e., Fig. 5(a), the oxidation reaction front). As shown in Fig. 5(b), discrete nanocrystals of several nanometers in size are observed within the region. However, the EDS mappings (Fig. 5(e)) show relatively uniform distributions of C and Ti, and the layered image of Hf and O (Figs. 5(c) and 5(d)) suggests the enrichment of Hf and O in the nanocrystals. In addition, Zr element distribution also assumed a slight enrichment tendency in nanocrystals. These results imply that the discrete tissues should be the crystal nuclei of the most thermodynamically favored Hf/Zr related oxides.

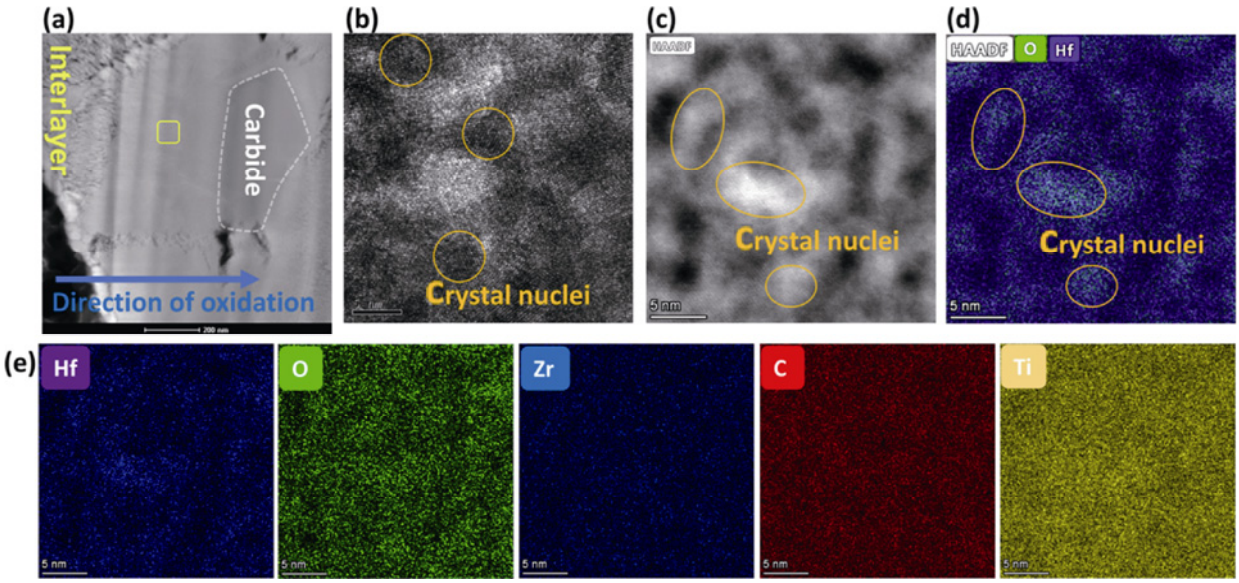

Fig. 5 (a) HAADF-STEM image of the region of the oxidation reaction front and (b) HRTEM image of the interlayer region adjacent to carbide (i.e., the yellow box in (a)). (c) Magnified HAADF-STEM view of the region. (d) HAADF-EDS layered image and (e) elemental mappings.

Such a process is illustrated in Fig. 4(e). With the proceeding of oxidation, more oxygen supplied, and the preferentially oxidized M_P will migrate from the unoxidized parts to the oxidizing microregion where oxide nucleated. Therefore, the nuclei of M_P-related oxide will develop into M_P-rich oxide skeleton; meanwhile, the "laggingly oxidized microregion" would become M_L-rich (Figs. 4(f) and 2(c)). Subsequently, these "laggingly oxidized microregion" will evolve into the infilling oxides rich in M_L of the skeleton (Figs. 4(g) and 3(a)). As for the Hf–Zr–Ti–C system, the structure of the "Hf/Zr-rich oxide skeleton infilled with the oxides rich in Ti" formed in this process. Furthermore, the compositional evolution should result from element migrations at mesoscale levels caused by preferential oxidation. As mentioned earlier, at nanoscale, the preferentially oxidized M_P (e.g., Hf/Zr) will migrate from the unoxidized microregion to the oxidizing microregion, forming the aforementioned microarchitecture. While, from the aspect of oxidation kinetics [31], the inward diffusion of O and the outward diffusion of metal cations dominate the oxidation process. Thus, at mesoscale level, due to the preferential oxidation of component-M_P, more M_P (e.g., Hf/Zr) would be oxidized than M_L (e.g., Ti). For instance, thermodynamic calculation (Tables S1 and S2 in the ESM) shows that more than 60 mol% Hf/Zr would be oxidized while most of Ti would be retained at 2620 K with 1 mol O_2. Under this circumstance, more M_L (e.g., Ti) would retain in the unoxidized microregion of the inner oxidizing region. Even though the Ti element is more prone to diffusing outwards due to its smaller atomic radius in this case [15], its less involvement in oxidation reduced its amount of outward-diffusion when compared to Hf/Zr. As a result, more M_P elements (e.g., Hf/Zr) diffused outward to the oxide of the outer oxidizing region, whereas more "lagging" M_L (e.g., Ti-species) would retain in the inner oxidizing region as oxidation proceeding. Consequently, M_L-content (e.g., Ti) in the interlayer and inner oxide scale gradually increased. This inference can be supported by the incremental concentration of Ti in amorphous phases with the distance from the oxidized surface and the increasing contents of Hf and Zr of oxide grains from interlayer to surface (Table 1). Noteworthy, such element distribution is consistent with the elemental line profiles (Fig. 2(b)). The compositional evolution process can also be illustrated by the schematic diagrams (Figs. 4(f)–4(h)).

4. 2 Method to predict the preferential oxidation and its temperature-dependence

The facile thermodynamic approach of comparative analysis of thermodynamic diagrams can also predict preferential oxidation in UHTCs though comparing the equilibrium $p(O_2)$ of different components. For instance, the significantly lower equilibrium $p(O_2)$ of HfC and ZrC than that of TiC indicates the preferential oxidation of Hf and Zr over Ti in the Hf–Zr–Ti–C

system at temperatures below 2735 K (Fig. 4(d)). Additionally, given the fact that the approach enables the analysis over an extended temperature range, it can also provide an integral description for the composition and phase evolution in the whole oxidation-affected zone of material that possesses a temperature–$p(O_2)$-gradient [4,32]. As reported in Ref. [33], the oxide scale formed on TiC at 1773.15 K and low $p(O_2)$ (0.08 kPa) is composed of outer subscale consisting of TiO_2 and the inner one containing Ti_3O_5 and carbon, which is in good agreement with the prediction of diagram for TiC. As shown in Fig. 4(c), the slash representing the composition evolution starts from the coordinate (1773.15, 1.90), and the slope of the slash represents the assumed temperature–$p(O_2)$-gradient. In this instance, the preferential oxidation of the metal elements over the carbon in the carbide case (i.e., the precipitation of carbon within the carbonaceous oxide interlayer, Fig. 2(d)) is predicted by the diagram. As the "MeO_2+C" zones (Figs. 4(a)–4(c)) in the diagram suggest, carbon "lagging" metal elements (i.e., Hf, Zr, and Ti) in the extent of oxidation will appear in a certain temperature–$p(O_2)$-range. Besides, the formation of this carbonaceous oxide interlayer could act as a primary oxygen diffusion barrier in carbide and be of great benefit to oxidation resistance. However, Refs. [3,24] rarely predicted the lagging oxidation of carbon.

Moreover, this facile thermodynamic approach also provides additional insight into the temperature-dependent nature of preferential oxidation. As indicated in the diagram (Fig. 4(d)), despite that HfC and ZrC are predicted to be preferentially oxidized over TiC at temperatures below 2735 K, the equilibrium $p(O_2)$ of HfC and ZrC are found to be higher than that of TiC (the red arrow and spot in Fig. 4(d)) when temperatures are higher than 2880 K. This suggests that the trend of preferential oxidation will reverse with increasing of temperature. Under this condition, TiC can be preferentially oxidized over HfC and ZrC. Besides, it was found that the equilibrium $p(O_2)$ of HfC is lower than that of ZrC over the entire studied temperature range. Thus, 2735 and 2880 K can be regarded as the transition temperatures of the preferential oxidation. Furthermore, these observations obtained from the thermodynamic diagram can be theoretically verified by the equilibrium calculation (Tables S1 and S2 in the ESM) at the corresponding temperatures.

In order to verify the analysis, an ablation test was conducted on the $Hf_{0.5}Zr_{0.3}Ti_{0.2}C$ at 3273.15 K. The extreme oxidation condition was realized by oxyacetylene ablation test. Relatively Ti-rich oxides were observed on the ablated surface (Fig. 6), which confirms that Ti can be preferentially oxidized over Hf/Zr at a temperature higher than 2880 K. However, the structure of Ti-rich oxide skeleton may not form in this high-temperature zone because the temperatures are remarkably higher than the melting point of most oxides, which would result in a molten oxide scale. Fundamentally, the transition of the tendency toward preferential oxidation can be ascribed to the relative difference in the standard Gibbs free energy of formation of the oxides at different temperatures [25]. Moreover, the elemental line profile across the oxidation-affected zone (including interlayer and oxide scale) appears to be more complex when ablation temperature exceeds 2880 K (Fig. 6). As shown in the cross-sectional EDS line profiles (Fig. 6(b)), there is a Hf-rich layer beneath the ablated surface and followed by a Ti-rich underlying layer. This composition evolution reflects the complex influence of the temperature-dependence. As indicated in Refs. [4,32], the temperature–$p(O_2)$-gradient would develop across the material during oxidation. Therefore, there will be a top layer where the local temperature is maintained at around 2880–3273.15 K. As predicted, Ti will be preferentially oxidized in this temperature region, yielding Ti-rich oxide (Fig. 6(d)) on the ablated surface and resulting in a gradually Hf-rich underlying region. This explains the existence of highly concentrated Hf/Zr beneath the external layer of oxide scale (Fig. 6(b)). While, beneath this layer, an interior part with a temperature below 2880 K is also speculated. However, according to the predictions, the trend of preferential oxidation would reverse in this interior part, which means that Hf/Zr would be preferentially oxidized. In this context, the interior part would become Ti-rich, just as the cross-sectional EDS line profiles depict (Fig. 6(b)).

More importantly, these results suggest that the compositional and structural evolution of the designed multicomponent system can be influenced by the oxidation temperature due to the temperature-dependent nature of the preferential oxidation. Also, the oxidation performance is affected. Therefore, the design of multicomponent system necessitates the consideration of its temperature applicability, and the transition temperature of preferential oxidation can offer a valuable reference.

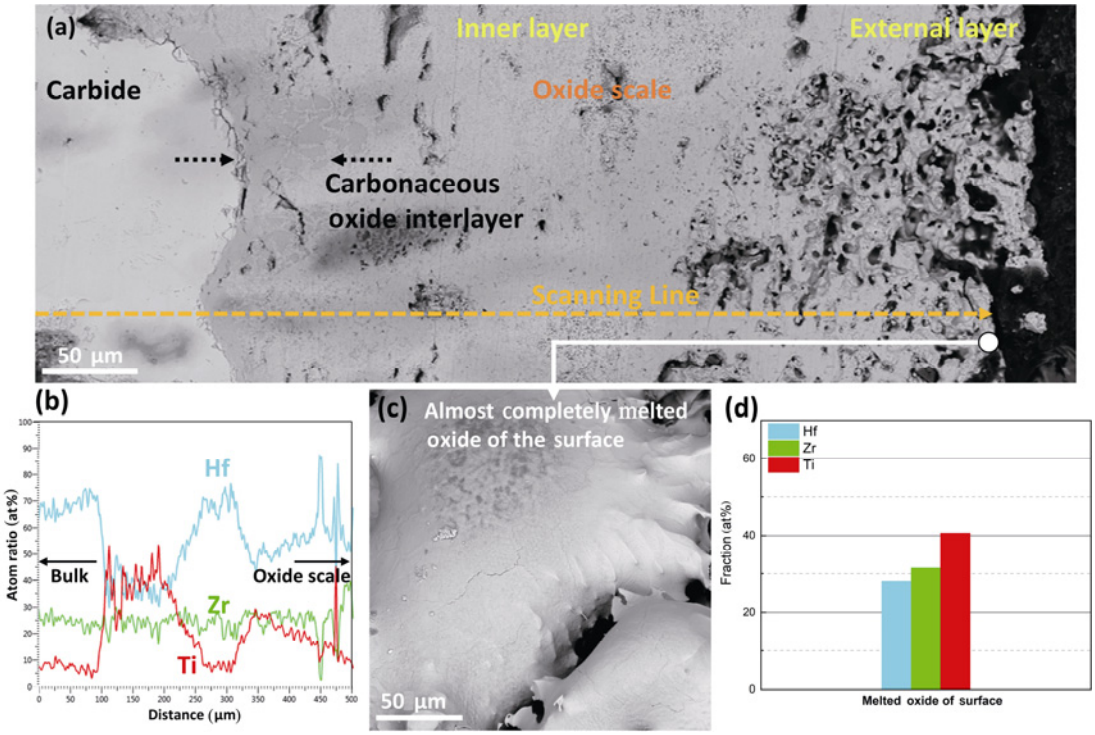

Fig. 6 (a) Cross-section of central region ablated at 3273.15 K, (b) cross-section EDS line profiles revealing metal element distributions, (c) SEM image of the surface of oxide scale, (d) corresponding composition analysis. All the results are averaged over three spots.

4. 3 Correlation between the components, oxidation behavior, and final performance

Having elucidated the role of preferential oxidation in ablation behavior of multicomponent UHTCs, the correlation between the components, ablation behavior, and final performance can be thus inferred. As previously analyzed, for a multicomponent system (denoted as M_P–M_L-containing system), the component elements can be broadly divided into M_P, which build up the oxide skeleton and the M_L, which constitute the infilling phase of the skeleton. Moreover, a gradual enrichment of the element-M_L with the depth of the oxide scale is also expected. Hence, the prediction of preferential oxidation in M_P–M_L-containing system was extended to a broader composition scope including group IV and V elements. As shown in Fig. 7, it is observed that the equilibrium $p(O_2)$ of group V components (Ta and Nb) are generally higher than those of group IV components (Hf, Zr, and Ti) within the entire studied temperature range, which suggests that group IV components can be preferentially oxidized over group V components in the carbide case. Moreover, the temperature-dependence of the preferential oxidation in the Ta-/Nb-containing system can also be analyzed, and their transition temperature of preferential oxidation can be identified as 2453 K. The detailed analysis is shown in Table S3 in the ESM.

Based on the predicted sequence of preferential oxidation of components (including Hf, Zr, Ti, Nb, and Ta) and the diagrams (Figs. 4(a)–4(c) and Figs. 7(a) and 7(b)), it is inferred that the M_P with relatively high melting points (e.g., Hf and Zr in Figs. 4(a) and 4(b)) are suitable for building a stable oxide skeleton at high temperatures. For instance, in the case of $Hf_{0.5}Zr_{0.3}Ti_{0.2}C$ ablated at 2620 K, Hf/Zr-rich oxides build up an adherent skeleton and remain solid at high temperatures [18,34]. While, the M_L with relatively low-melting points (e.g., Ti, Nb, and Ta in Figs. 4(c), 7(a), and 7(b)) are appropriate candidates for component-M_L. Because they can *in-situ* melt and fill the pores and defects within grain skeleton, such as the Ti rich phase within Hf/Zr-rich oxide skeleton in the $Hf_{0.5}Zr_{0.3}Ti_{0.2}C$ [18]. Thus, the formation of the protective structure of oxide skeleton filled with healing phase is largely attributed the collaboration of preferential oxidation and the intrinsic thermophysical properties of the oxidation products. Meanwhile, the addition of M_L with a relatively low melting point should be limited, because their enrichment within the inner oxide layer may

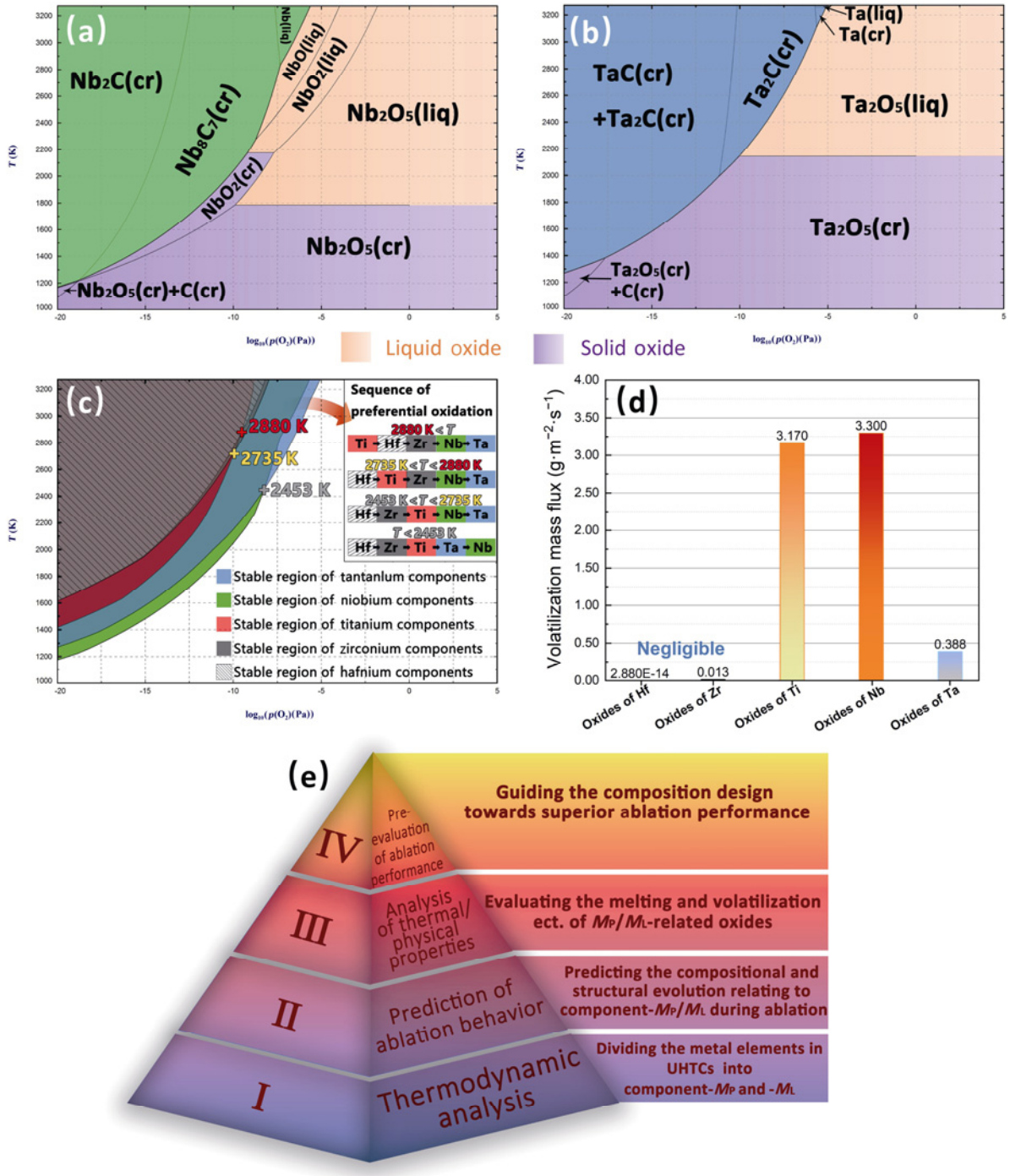

Fig. 7 Condensed phase equilibrium diagrams of (a) NbC and (b) TaC. (c) Compiled condensed phase equilibrium diagram of HfC–ZrC–TiC–TaC–NbC. (d) Volatilization mass fluxes of the volatile species under 2700 K and $p(O_2)$ = 20,265 Pa (i.e., 0.2 atm, $p(O_2)$ in atmosphere). (e) Diagram showing the strategy for pre-evaluating the ablation performance of multicomponent UHTCs.

lower the melting point and the temperature capability of the oxide scale according to the phase diagrams. Hence, in Ref. [18], the Ti-content of the multicomponent system (i.e., Hf–Zr–Ti–C) which was designed to be 20 at% and exhibited a significant improvement in ablation performance. Moreover, some factors such as viscosity and catalytic coefficient of the oxides would also affect the final oxidation performance. It is indicated that oxides with a very high viscosity (e.g., no melt) or liquid oxide with a very low viscosity (e.g., freely flowing) may detach or splash from the oxide skeleton, decreasing the protectiveness of the oxide layer. Ref.

[4] shows that the molten oxide of relatively Ti-rich oxides possesses a suitable viscosity, which could seal the defects and protect the matrix well. Moreover, under a plasma environment, surface catalysis would occur and cause a large increment of surface heat flux, and thus lead to more severe ablation [35]. Therefore, the as-formed oxides with minor catalytic coefficient are preferable for achieving better ablation resistance.

It can be concluded that the oxidation performance of the multicomponent UHTCs is the combination of the following factors. Firstly, the high-temperature capability of the oxides of M_P will determine the stability of the protective oxide scale, while the melt-forming ability of the oxides of M_L may significantly impact the self-healing ability of the material. Secondly, the content of M_L with a relatively low melting point will affect the temperature capability of the oxide scale. Furthermore, given the relatively higher vapor pressures of the oxides associated with M_L (e.g., TiO, TiO_2, NbO_2, and TaO_2), the as-formed M_L-rich oxides will lead to the volatility loss of material. Besides, viscosity and catalytic coefficient of the oxide should also be concerned.

4. 4 Strategy for pre-evaluating the ablation performance of multicomponent UHTCs

Based on the tendency of preferential oxidation and correlation, the ablation performance of multicomponent systems can be pre-evaluated, and we summarize the pre-evaluation strategy in Fig. 7(e). Herein, based on the previous investigations on $Hf_{0.5}Zr_{0.3}Ti_{0.2}C$ [18,36], $Hf_{0.5}Zr_{0.3}Ti_{0.1}Ta_{0.1}C$ (Ta-doped system) and $Hf_{0.5}Zr_{0.3}Ti_{0.1}Nb_{0.1}C$ (Nb-doped system) are designed as the representative multicomponent systems for the pre-evaluation and comparison.

According to the elucidation of the role of preferential oxidation, the Hf/Zr-rich oxide skeleton is supposed to form on the three multicomponent systems mentioned above. Considering the relatively high catalytic coefficient of HfO_2 (higher than that of ZrO_2), the ablated surfaces of samples would reach relatively high temperatures [35,37,38]. And gradually enrichment of Ta and Nb is expected to appear within the oxide scale on the Ta-doped and Nb-doped systems. Based on the phase diagrams [27,28,39,40] and condensed phase equilibrium diagrams shown in Figs. 4(a)–4(c) and Figs. 7(a) and 7(b), the Nb-containing oxide scale is predicted to possess a relatively lower melting point. At the same time, the melting point of the Ta-containing oxide scale might be similar to that of the oxide scale formed on $Hf_{0.5}Zr_{0.3}Ti_{0.2}C$. Therefore, it can be inferred that the high-temperature capability of the oxide scale of $Hf_{0.5}Zr_{0.3}Ti_{0.1}Nb_{0.1}C$ may be inferior to that of $Hf_{0.5}Zr_{0.3}Ti_{0.1}Ta_{0.1}C$ and $Hf_{0.5}Zr_{0.3}Ti_{0.2}C$. In addition, during ablation, Ta-rich and Nb-rich phases will melt and infill the pores and defects within oxide skeleton of the Ta-doped and Nb-doped systems at similar oxidation temperatures, respectively [3]. Thus, both Ta-doped and Nb-doped systems can achieve self-healing similar to the $Hf_{0.5}Zr_{0.3}Ti_{0.2}C$ system. Under this circumstance, the volatile depletion of the low-melting Ti-/Ta-/Nb-rich infilling phase with enrichment tendency can, to a great extent, determine the volatility loss of these multicomponent systems.

In order to evaluate the volatility loss caused by each component quantitatively, Langmuir equation [41–43] was applied here:

$$J_{\mathrm{vap},i} = p_{\mathrm{vap},i}\left(\frac{M_i}{2\pi RT}\right)^{1/2} \tag{3}$$

where $p_{\mathrm{vap},i}$ (Pa) is the vapor pressure, M_i ($\mathrm{g\cdot mol^{-1}}$) is the molar mass of vapor species i, R ($\mathrm{J\cdot K^{-1}\cdot mol^{-1}}$) is the universal gas constant, and T (K) is the temperature. The calculated results of volatilization mass flux ($\mathrm{g\cdot m^{-2}\cdot s^{-1}}$), i.e., $J_{\mathrm{vap},i}$, represent the mass transfer rate within the surface layer constantly attenuated by the high-speed flushing, which is applicable for oxidizing scenarios of ablation in this work. The Ta-, Nb-, Ti-, Zr-, and Hf-related volatile species under oxidizing environment are summarized in Fig. 7(d) and Table S4 in the ESM based on FactSage 7.3. Moreover, their equilibrium partial pressures were calculated by the Equilibrium Module. Given the experimental conditions, the temperature and $p(O_2)$ were extended to 2700 K and 20,265 Pa (i.e., 0.2 atm, the $p(O_2)$ in THE atmosphere), respectively, for the convenience of comparison. According to the results listed in Table S4 in the ESM, the total volatilization mass fluxes of Hf- and Zr-species are, at least, 13 and 1 orders of magnitude lower than those of other components, demonstrating the considerable thermal stability of Hf- and Zr-related oxide.

More importantly, the total volatilization mass flux of Ta-related species is approximately ten times lower than that of Ti, while the total volatilization mass flux of Nb-related species is quite close to that of Ti. Thus, it is believed that the total volatility loss of Ta-doped

system should be reduced by forming a gradually Ta-rich oxide scale, in which less volatile Ta-rich oxide phases formed instead of relatively more volatile Ti-rich oxide phases. Therefore, comparing to the $Hf_{0.5}Zr_{0.3}Ti_{0.2}C$ system, a better ablation resistance of $Hf_{0.5}Zr_{0.3}Ti_{0.1}Ta_{0.1}C$ is expected. Nevertheless, doping Nb into the Hf–Zr–Ti–C system may not be able to reduce the total volatility loss because of the unreduced total volatilization. Besides, it is believed that the viscosity Ta_2O_5 at the melting point is lower than that of TiO_2, while the viscosity Nb_2O_5 is even lower than that of Ta_2O_5 [44–47]. This decremental of viscosity of molten phase might also weaken the protectiveness of the oxide layer. Furthermore, considering the possible reduced melting point of the skeleton, it can be also pre-evaluated that the Nb-doped system is unlikely to achieve a substantial improvement in ablation resistance.

4. 5 Experimental verification on the pre-evaluation of ablation performance

Experimental verification was conducted on $Hf_{0.5}Zr_{0.3}Ti_{0.1}Ta_{0.1}C$ and $Hf_{0.5}Zr_{0.3}Ti_{0.1}Nb_{0.1}C$ (the microstructures and compositions of these two carbides are demonstrated in Fig. S4 and the text in the ESM). Then these two multicomponent carbides were subject to a plasma ablation test with identical parameters. During the test, the $Hf_{0.5}Zr_{0.3}Ti_{0.1}Nb_{0.1}C$ and $Hf_{0.5}Zr_{0.3}Ti_{0.1}Ta_{0.1}C$ achieves a temperature of 2540 K (Fig. 8(a)). The three carbides (including $Hf_{0.5}Zr_{0.3}Ti_{0.2}C$) reached a similar temperature. The slight temperature difference is possibly due to the differences in emissivity or thermal conductivity of the oxide layers. Generally, low LAR and MAR values suggest that the oxide layer expands and the mass gain exceeds the mass loss caused by ablation, implying minor mass consumption

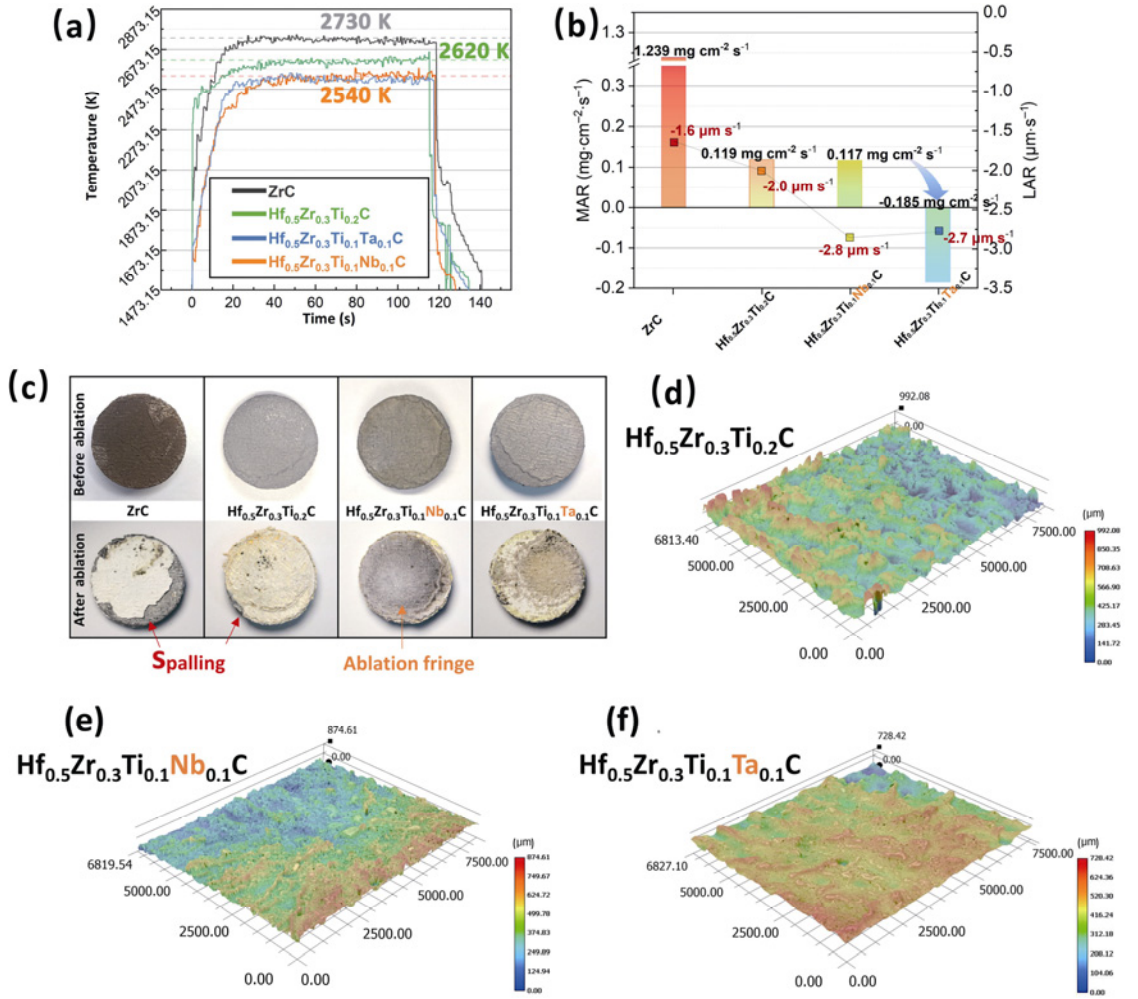

Fig. 8 (a) Temperature as a function of ablation duration recorded from the sample's surface. (b) Comparison of performance (MAR and LAR) of ZrC, $Hf_{0.5}Zr_{0.3}Ti_{0.2}C$, $Hf_{0.5}Zr_{0.3}Ti_{0.1}Nb_{0.1}C$, and $Hf_{0.5}Zr_{0.3}Ti_{0.1}Ta_{0.1}C$. (c) Morphologies of samples before and after ablation. (d–f) Surface profiles of central region of ablated samples.

and excellent dimensional stability of the tested materials. Notably, the 10 at% Ta-doped system (i.e., $Hf_{0.5}Zr_{0.3}Ti_{0.1}Ta_{0.1}C$) demonstrates a remarkable improvement in ablation resistance. The both negative values of LAR and MAR obviously distinguish it from other UHTCs indicated by the blue arrows in Fig. 8(b), indicating that a good quality protective oxide layer of carbide is formed during the ablation test. The mass loss rate of $Hf_{0.5}Zr_{0.3}Ti_{0.1}Ta_{0.1}C$ is more than 250% lower than that of $Hf_{0.5}Zr_{0.3}Ti_{0.2}C$ and is an order of magnitude lower than that of conventional ZrC material. However, the mass loss rate of the Nb-doped system (i.e., $Hf_{0.5}Zr_{0.3}Ti_{0.1}Nb_{0.1}C$) is almost equal to that of the $Hf_{0.5}Zr_{0.3}Ti_{0.2}C$ system. Particularly, it is observed that the ablated surfaces of $Hf_{0.5}Zr_{0.3}Ti_{0.1}Ta_{0.1}C$ are relatively smooth and intact, which is in contrast to the rougher ablated surface of $Hf_{0.5}Zr_{0.3}Ti_{0.2}C$ and $Hf_{0.5}Zr_{0.3}Ti_{0.1}Nb_{0.1}C$ (Figs. 8(c)–8(e)). Besides, the conventional ZrC material appeared catastrophically spalling. In summary, the experimental verification, at the macro level, confirms the pre-evaluation that doping Ta into the Hf–Zr–Ti–C system can substantially improve the oxidation performance but Nb-doping cannot. A multicomponent carbide, $Hf_{0.4375}Zr_{0.2625}Ti_{0.3}C$, which possess a higher Ti-content was also ablated under the identical environment, and the Hf/Zr ratio is identical to that of $Hf_{0.5}Zr_{0.3}Ti_{0.2}C$. However, its MAR and LAR are 2.753 $mg \cdot s^{-1} \cdot cm^{-2}$ and 4.76 $\mu m \cdot s^{-1}$, respectively, which is an order of magnitude higher than that of $Hf_{0.5}Zr_{0.3}Ti_{0.2}C$. As indicated earlier, this is because of the enrichment of the M_L (i.e., Ti) within the inner oxide layer that greatly lowers the melting point and the temperature capability of the oxide scale. And its ablation morphology and structure shown in Fig. S5 in the ESM further confirm the inference.

Moreover, the detailed experimental observations are consistent to the predicted compositional and structural evolution. First, at the nano-scale level, as the STEM micrographs (Figs. 9(a)–9(e) and 10(a)–10(e)) present, oxides indexed to be monoclinic oxide (obtained with

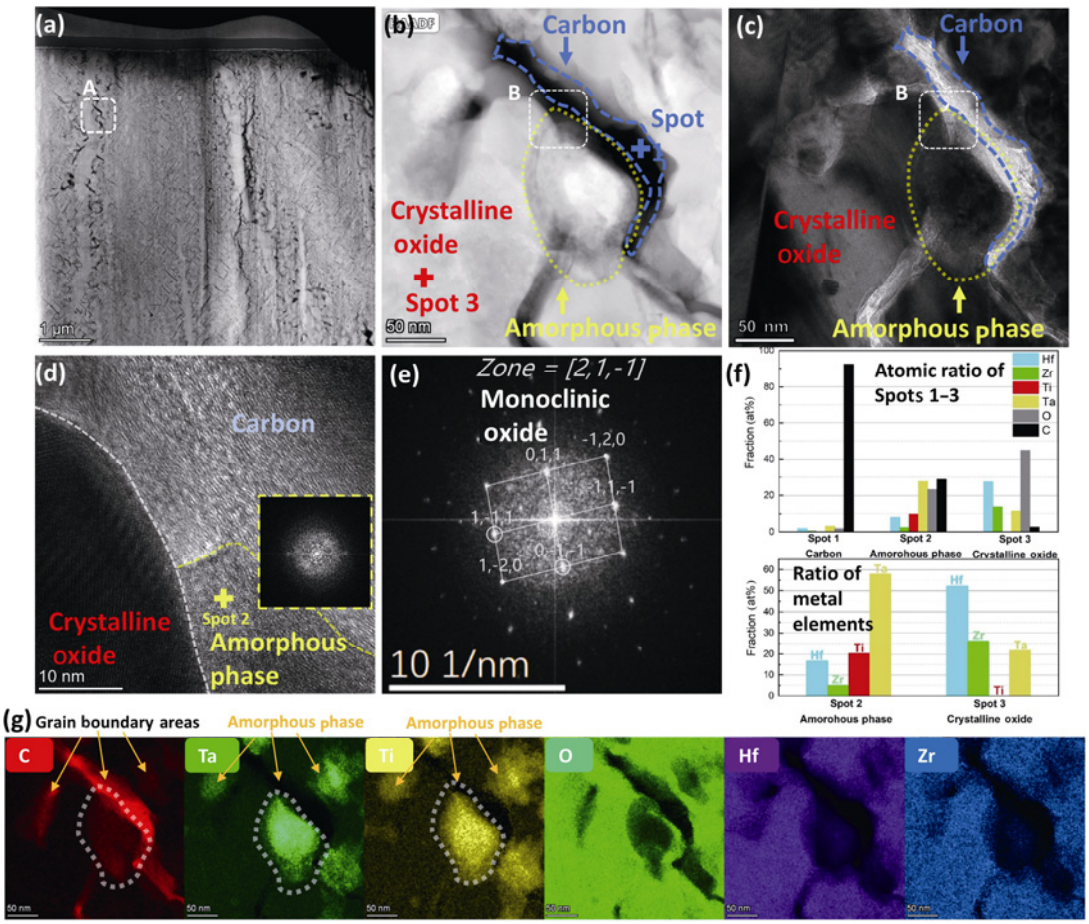

Fig. 9 (a) HAADF-STEM image of the oxidized region at the interlayer of $Hf_{0.5}Zr_{0.3}Ti_{0.1}Ta_{0.1}C$, (b, c) magnified HAADF-STEM view and TEM view of region A in (a), respectively, (d) high-magnification image of region B in (c) (the inset is the FFT pattern), (e) FFT pattern of the crystalline oxide, (f) EDS analysis on the three spots, and (g) EDS elemental mappings of region A in (a).

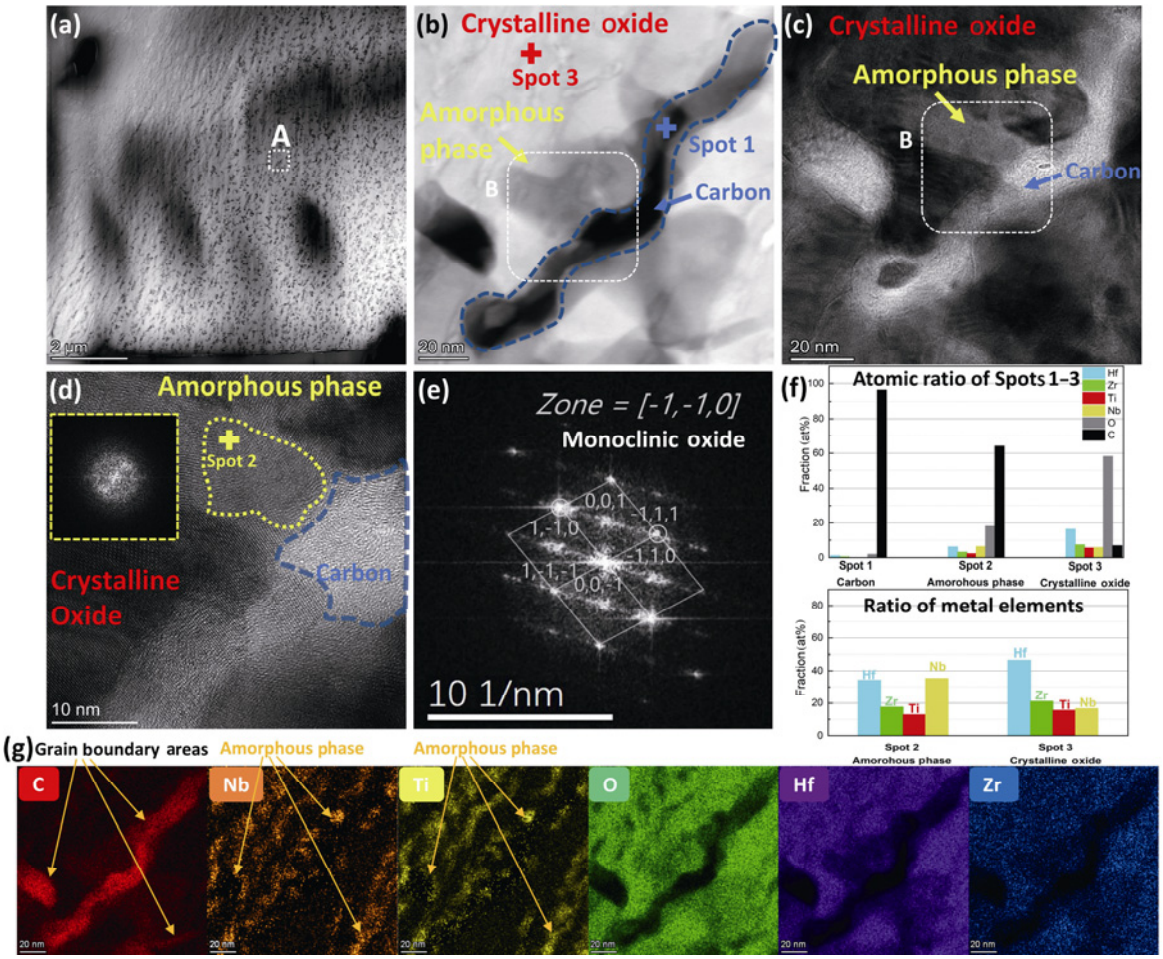

Fig. 10 (a) HAADF-STEM image of the oxidized region at the interlayer of $Hf_{0.5}Zr_{0.3}Ti_{0.1}Nb_{0.1}C$, (b, c) magnified HAADF-STEM view and TEM view of region A in (a), respectively, (d) high-magnification image of region B in (c) (the inset is the FFT pattern), (e) FFT pattern of the crystalline oxide, (f) EDS analysis on the three spots and (g) EDS elemental mappings of region A in (a).

HfO_2, JCPDS 43-1017, Figs. 9(a)–9(e) and 10(a)–10(e)) constitute grain skeletons (the TEM slices were lifted out from the carbonaceous oxide interlayers of ablated samples, Figs. S3(b) and S3(c) in the ESM). The STEM–EDS analysis (Spot 3 in Figs. 9(f), 9(g), 10(f), and 10(g)) proves that the oxide skeletons are Hf/Zr-enriched. Meanwhile, it can be inferred from the HRTEM and EDS results (Figs. 9(d), 9(f), 9(g), 10(d), 10(f), and 10(g) that some amorphous phases, gathering at grain boundaries and spaces (Figs. 9(d), 9(f), 10(d), and 10(f)), are Ta/Ti-rich or Nb/Ti-rich phases and probably contain part of carbon. Whilst, carbon with typical layered graphite structure is observed along the grain boundary areas from the HRTEM results (Figs. 9(c), 9(d), 10(c), and 10(d)) and the STEM–EDS analysis (Spot 1 in Figs. 9(f), 9(g), 10(f), and 10(g)). As the oxide skeletons are Hf/Zr-enriched, the partially oxidized carbon-enriched areas correspond with the enrichment of Ta/Ti or Nb/Ti (Spot 2 in Figs. 9(f), 9(g), 10(f), and 10(g)), while the enrichment tendency of Ta and Nb are found to be more pronounced than that of Ti. This result is in good agreement with the predicted preferential oxidation of group IV elements.

The SEM images of the cross-section of the ablated regions reveal that the Nb-doped system possesses an inner oxide scale with obvious pores (Fig. 12(c)). While, the inner oxide layer of the Ta-doped system remains nearly intact, almost free from the voids (Fig. 12(a)), demonstrating the less volatilization of its oxide layer. And the carbonaceous oxide interlayers are detected within both two systems (Figs. 12(a) and 12(c)). Moreover, comparing the central-ablated surface (Figs. 11(a) and 11(f)) of these two carbides with the $Hf_{0.5}Zr_{0.3}Ti_{0.2}C$ (Fig. 1(d)), the holes existing on the surface are found to shrink evidently, implying more melting of the Ta- and Nb-related oxides due to the possibly lower melting points and viscosities. Meanwhile, the oxide scale of the Nb-doped system exhibits more obvious

melting than those of the Ta-doped system and $Hf_{0.5}Zr_{0.3}Ti_{0.2}C$ (Fig. 8(b), ablation fringe). These observations confirm the inferior high-temperature capability of the oxide scale of the Nb-doped system.

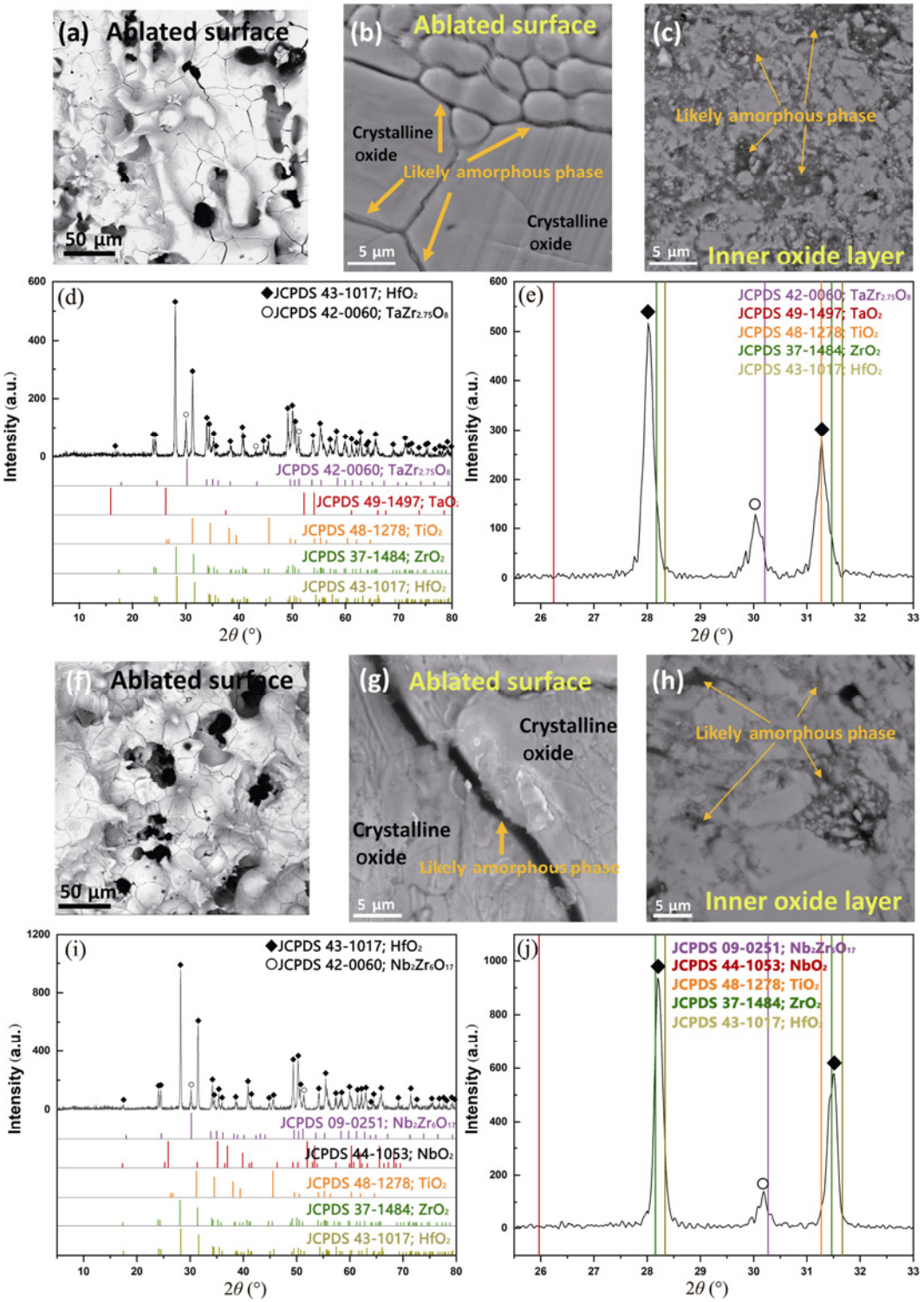

Fig. 11 SEM images (backscattered electron) and XRD patterns of central-ablated surfaces of (a, d) $Hf_{0.5}Zr_{0.3}Ti_{0.1}Ta_{0.1}C$ and (f, i) $Hf_{0.5}Zr_{0.3}Ti_{0.1}Nb_{0.1}C$. The magnified patterns at (−111) and (111) and peak positions of pristine oxides of $Hf_{0.5}Zr_{0.3}Ti_{0.1}Ta_{0.1}C$ and $Hf_{0.5}Zr_{0.3}Ti_{0.1}Nb_{0.1}C$ are shown in (e) and (j), respectively. SEM images (secondary electron) of the magnified central surface oxide layer of (b) $Hf_{0.5}Zr_{0.3}Ti_{0.1}Ta_{0.1}C$ and (g) $Hf_{0.5}Zr_{0.3}Ti_{0.1}Nb_{0.1}C$. SEM images (backscattered electron) of the inner oxide layer of (c) $Hf_{0.5}Zr_{0.3}Ti_{0.1}Ta_{0.1}C$ and (h) $Hf_{0.5}Zr_{0.3}Ti_{0.1}Nb_{0.1}C$.

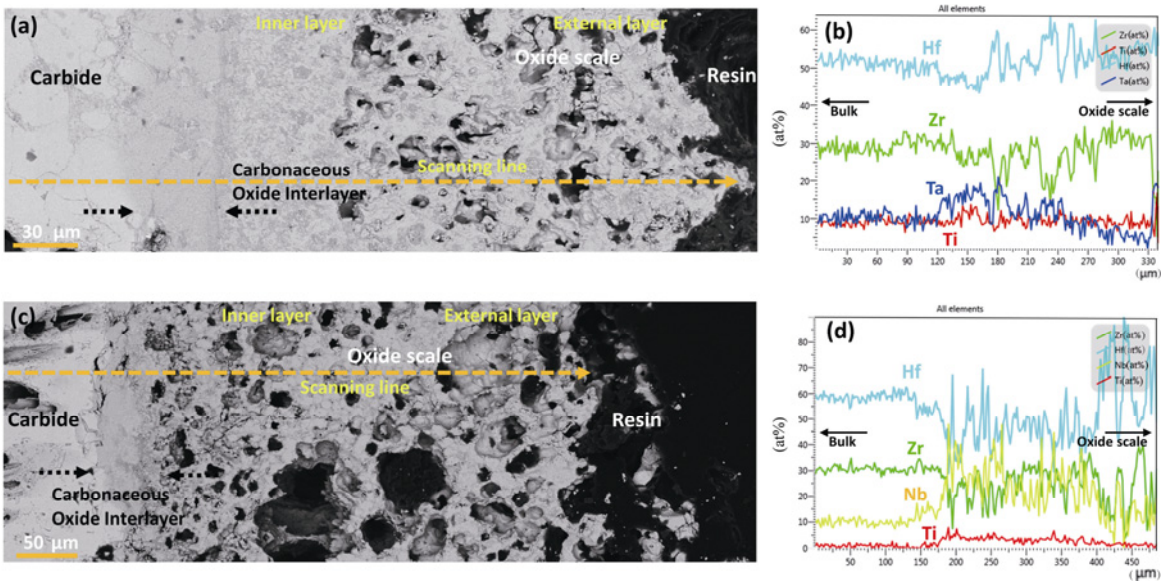

Fig. 12 SEM image of cross-section of the central-ablated region of (a) $Hf_{0.5}Zr_{0.3}Ti_{0.1}Ta_{0.1}C$ and (c) $Hf_{0.5}Zr_{0.3}Ti_{0.1}Nb_{0.1}C$. Cross-section EDS line profiles reveal metal element distributions of (b) $Hf_{0.5}Zr_{0.3}Ti_{0.1}Ta_{0.1}C$ and (d) $Hf_{0.5}Zr_{0.3}Ti_{0.1}Nb_{0.1}C$.

As shown in the XRD patterns (Figs. 11(d), 11(e), 11(i), and 11(j)), two sets of peaks are indexed to monoclinic HfO_2 (JCPDS 43-1017) with a small shift to a lower angle that suggests the formation of multicomponent oxide solid solutions. Also, the peaks of $TaZr_{2.75}O_8$ (JCPDS 42-0060) and $Nb_2Zr_6O_{17}$ (JCPDS 09-0251) confirm the formation of some Ta-rich and Nb-rich oxides on the ablated surface. As Figs. 11(b) and 11(g) and the corresponding EDS analysis (Table S5 in the ESM) suggest, for both Nb-doped and Ta-doped systems, a similar structure of "Hf/Zr-rich oxide skeleton infill with Ta-rich or Nb-rich phases" can be detected within the ablated surface, as well as the inner oxide layer (Figs. 11(c) and 11(h) and Table S5 in the ESM).

In addition, consistent with the prediction, composition evolution of gradual enrichment of Ta/Nb with the depth of oxide scale appears in the multicomponent systems, as the Ta and Nb concentrations are found to gradually increase in the EDS line profiles (Figs. 12(b) and 12(d), respectively). Meanwhile, these enrichment tendencies are found to be more pronounced than that of Ti. Under this condition, Ta- or Nb-rich oxides within the oxide scale would become the major volatile species instead of the Ti-rich oxides. Therefore, it is validated that the improvement of ablation resistance of the Ta-doped system is largely credited to the retained high-temperature capability of the oxide scale and reduced volatile consumption of the material. More importantly, this shows that superior ablation performance of multicomponent UHTCs can be achieved by desirable thermodynamic design and pre-evaluation.

4. 6 Insights on the composition and component ratio design of multicomponent UHTCs

On the basis of the above thermodynamic studies and experimental investigations, prospective analysis can also be conducted on the oxidation behaviors of group IV- and V-containing multicomponent diborides and nitrides. Their condensed phase equilibrium diagrams (Figs. S6 and S7 in the ESM) are constructed, and then integrated into compiled diagrams (Fig. 13). The tendency toward preferential oxidation is found to be similar to that of carbide (Fig. 7(c)). Detailed description is presented in the text and Figs. S6 and S7 in the ESM.

More broadly, preliminary remarks can be made on the composition and component ratio design of multicomponent UHTCs based on the elucidation of the role of preferential oxidation and the strategy (Fig. 7(e)). Firstly, the M_P in UHTCs will preferentially nucleate and further form M_P-rich oxide skeleton infilled with the oxides rich in M_L. Thus, the desirable composition design is to select the preferentially oxidized elements, whose oxides have a higher melting point (e.g., Hf, Zr, etc.) as component-M_P, while the laggingly oxidized elements, which can derive relatively low-melting oxides (e.g., Ti, Nb, Ta, etc.) should be selected as component-M_L. Such composition design is conducive to the formation of a protective structure of "stable oxide skeleton infilled with melts" in oxide scale at high temperatures.

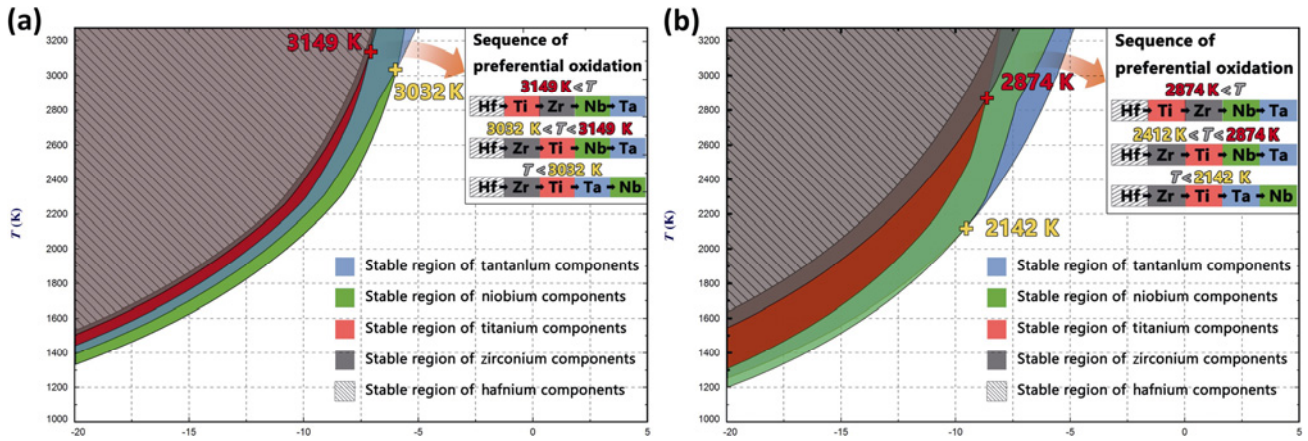

Fig. 13 Compiled condensed phase equilibrium diagrams of group IV and V element-based (a) borides and (b) nitrides.

In addition, during oxidation, M_P would migrate outward more pronounce than M_L due to the preferential oxidation of M_P, resulting in a gradually M_L-rich oxide scale. Therefore, the ratio of the low-melting component-M_L should be limited based on phase diagrams, or their high concentrations in the inner oxide layer may reduce the high-temperature capability of the oxide scale. More importantly, the relatively low-melting oxidation products of component-M_L will necessarily result in volatility loss of material. Therefore, exploiting laggingly oxidized elements, whose oxides possess lower volatilization rate to substitute that with a relatively higher volatilization rate, can reduce the volatile consumption thereby alleviating the material loss. Besides, the viscosity of these oxides should also be concerned, because the oxides with a very high viscosity (e.g., no melt) or liquid oxide with a very low viscosity (e.g., freely flowing) may detach or splash from the oxide skeleton, decreasing the protectiveness of the oxide layer. Actually, the design of component-M_L requires a trade-off between melt-forming ability, temperature capability, viscosity, and volatilization loss. In most cases, the collaboration of multiple elements is needed to realize this purpose effectively. For instance, the co-doping of Ti and Ta in the present work (i.e., the Hf–Zr–Ti–Ta–C) evidently enhanced the ablation resistance of the designed multicomponent system. This also reveals the necessity of development towards multicomponent UHTCs.

Also, the application temperature of the designed multicomponent system should be concerned, as the tendency toward preferential oxidation can be reversed when temperatures exceed the transition point, which will greatly affect the favorable compositional and structural evolution. Moreover, for the multicomponent system applied in the oxidizing environment with temperatures exceed the transition points, the co-doping of group IV components with a high melting point (e.g., Hf and Zr) and group V components, which can derive relatively low-melting oxides (e.g., Ta), is a reasonable designing strategy. Because group IV components would be preferentially oxidized over group V components within a broader temperature range that is almost independent of the transition points. Moreover, from the aspect of the temperature capability, given the gradually enrichment tendency of M_L oxides with relatively low-melting points in the outer oxide scale, the ratio of the low-melting M_L should be further reduced based on phase diagrams. In addition, the content of the component with a high melting point (e.g., Hf or Zr) should be increased in order to further guarantee the temperature capability at the elevated temperatures. However, considering the relatively high catalytic coefficient of HfO_2 (higher than that of ZrO_2), the design of component-M_p also requires a trade-off between temperature capability and catalytic coefficient. Besides, the selection of appropriate component-M_L to reduce the volatile consumption is also important, and can refer to that of the composition design at the temperatures below the transition point.

5 Conclusions

In this work, the correlation between the composition and ablation performance of multicomponent UHTCs was revealed through elucidating the role of preferential oxidation in ablation behavior. It is found that the metal components in UHTCs can be thermodynamically divided into M_P, which builds up a skeleton in oxide

layer, and M_L, which fills the oxide skeleton. Meanwhile, a thermodynamically driven gradient in concentration of M_P and M_L forms in the oxide layer. It is also found that the tendency of preferential oxidation of components will reverse with increasing temperatures. Importantly, an approach for pre-evaluating the ablation properties of multicomponent UHTCs is proposed. In this approach, thermodynamic diagrams are used to determine the sequence of preferential oxidation of components at ablation temperature. Combining the analysis of thermophysical properties of component-M_p and M_L, the ablation performance of multicomponent UHTCs with different metal compositions or component ratios can be pre-evaluated. The approach was experimentally validated in representative multicomponent UHTCs, which provides a preliminary basis for the composition and component ratio design of multicomponent UHTCs (including high-entropy ceramics).

Acknowledgements

This work was supported by the National Natural Science Foundation of China (52072410 and 51602349) and Innovation-driven Project of Central South University. The authors would like to thank Qiankun Yang (Central South University) for the TEM analysis and Jingli Liu (Xidian University) for the assistance in the data processing of thermodynamic calculations.

Author contributions

Xiang Xiong and Yi Zeng proposed and designed the project. Ziming Ye fabricated the multicomponent ceramics and analysed them by the SEM and TEM. Ziming Ye also developed the approach for pre-evaluating the ablation performance of multicomponent UHTCs. Huilin Lun carried out the XRD and analyses. Ziming Ye wrote the paper with input from all authors, and Xiang Xiong, Yi Zeng, and Qingbo Wen refined the paper. All authors contributed to the interpretation of the results.

Declaration of competing interest

The authors have no competing interests to declare that are relevant to the content of this article.

Electronic Supplementary Material

Supplementary material is available in the online version of this article at https://doi.org/10.1007/s40145-022-0659-2.

References

[1] Gild J, Zhang YY, Harrington T, *et al*. High-entropy metal diborides: A new class of high-entropy materials and a new type of ultrahigh temperature ceramics. *Sci Rep* 2016, **6**: 37946.

[2] Harrington TJ, Gild J, Sarker P, *et al*. Phase stability and mechanical properties of novel high entropy transition metal carbides. *Acta Mater* 2019, **166**: 271–280.

[3] Backman L, Opila EJ. Thermodynamic assessment of the group IV, V and VI oxides for the design of oxidation resistant multi-principal component materials. *J Eur Ceram Soc* 2019, **39**: 1796–1802.

[4] Zeng Y, Wang DN, Xiong X, *et al*. Ablation-resistant carbide $Zr_{0.8}Ti_{0.2}C_{0.74}B_{0.26}$ for oxidizing environments up to 3,000 ℃. *Nat Commun* 2017, **8**: 15836.

[5] Nisar A, Zhang C, Boesl B, *et al*. A perspective on challenges and opportunities in developing high entropy- ultra high temperature ceramics. *Ceram Int* 2020, **46**: 25845–25853.

[6] Wright AJ, Wang QY, Huang CY, *et al*. From high-entropy ceramics to compositionally-complex ceramics: A case study of fluorite oxides. *J Eur Ceram Soc* 2020, **40**: 2120–2129.

[7] Feng L, Fahrenholtz WG, Brenner DW. High-entropy ultra-high-temperature borides and carbides: A new class of materials for extreme environments. *Annu Rev Mater Res* 2021, **51**: 165–185.

[8] Dusza J, Švec P, Girman V, *et al*. Microstructure of (Hf–Ta–Zr–Nb)C high-entropy carbide at micro and nano/atomic level. *J Eur Ceram Soc* 2018, 38: 4303–4307.

[9] Ma MD, Hu XF, Meng H, *et al*. High-entropy metal carbide nanowires. *Cell Rep Phys Sci* 2022, **3**: 100839.

[10] Ma MD, Sun YA, Wu YJ, *et al*. Nanocrystalline high-entropy carbide ceramics with improved mechanical properties. *J Am Ceram Soc* 2022, **105**: 606–613.

[11] Yan XL, Constantin L, Lu YF, *et al*. $(Hf_{0.2}Zr_{0.2}Ta_{0.2}Nb_{0.2}Ti_{0.2})C$ high-entropy ceramics with low thermal conductivity. *J Am Ceram Soc* 2018, **101**: 4486–4491.

[12] Ren K, Wang QK, Shao G, *et al*. Multicomponent high-entropy zirconates with comprehensive properties for advanced thermal barrier coating. *Scripta Mater* 2020, **178**: 382–386.

[13] Zhao ZF, Xiang HM, Dai FZ, *et al*. $(La_{0.2}Ce_{0.2}Nd_{0.2}Sm_{0.2}Eu_{0.2})_2Zr_2O_7$: A novel high-entropy ceramic with low thermal conductivity and sluggish grain growth rate. *J Mater Sci Technol* 2019, **35**: 2647–2651.

[14] Ye BL, Wen TQ, Nguyen MC, *et al*. First-principles study, fabrication and characterization of $(Zr_{0.25}Nb_{0.25}Ti_{0.25}V_{0.25})C$ high-entropy ceramics. *Acta Mater* 2019, **170**: 15–23.

[15] Ye BL, Wen TQ, Liu D, *et al*. Oxidation behavior of $(Hf_{0.2}Zr_{0.2}Ta_{0.2}Nb_{0.2}Ti_{0.2})C$ high-entropy ceramics at 1073–1473 K in air. *Corros Sci* 2019, **153**: 327–332.

[16] Zhou JY, Zhang JY, Zhang F, *et al*. High-entropy carbide: A novel class of multicomponent ceramics. *Ceram Int* 2018, **44**: 22014–22018.

[17] Lipke DW, Ushakov SV, Navrotsky A, *et al*. Ultra-high temperature oxidation of a hafnium carbide-based solid solution ceramic composite. *Corros Sci* 2014, **80**: 402–407.
[18] Ye ZM, Zeng Y, Xiong X, *et al*. New insight into the formation and oxygen barrier mechanism of carbonaceous oxide interlayer in a multicomponent carbide. *J Am Ceram Soc* 2020, **103**: 6978–6990.
[19] Lun HL, Zeng Y, Xiong X, *et al*. Oxidation behavior of non-stoichiometric $(Zr,Hf,Ti)C_x$ carbide solid solution powders in air. *J Adv Ceram* 2021, **10**: 741–757.
[20] Ni DW, Cheng Y, Zhang JP, *et al*. Advances in ultra-high temperature ceramics, composites, and coatings. *J Adv Ceram* 2022, **11**: 1–56.
[21] Xiang HM, Xing Y, Dai FZ, *et al*. High-entropy ceramics: Present status, challenges, and a look forward. *J Adv Ceram* 2021, **10**: 385–441.
[22] Lun HL, Yuan JH, Zeng Y, *et al*. Mechanisms responsible for enhancing low-temperature oxidation resistance of nonstoichiometric (Zr,Ti)C. *J Am Ceram Soc* 2022, **105**: 5309–5324.
[23] Wang YC, Zhang RZ, Zhang BH, *et al*. The role of multi-elements and interlayer on the oxidation behaviour of (Hf–Ta–Zr–Nb)C high entropy ceramics. *Corros Sci* 2020, **176**: 109019.
[24] Backman L, Gild J, Luo J, *et al*. Part I: Theoretical predictions of preferential oxidation in refractory high entropy materials. *Acta Mater* 2020, **197**: 20–27.
[25] Backman L, Gild J, Luo J, *et al*. Part II: Experimental verification of computationally predicted preferential oxidation of refractory high entropy ultra-high temperature ceramics. *Acta Mater* 2020, **197**: 81–90.
[26] Lun HL, Zeng Y, Xiong X, *et al*. Synthesis of carbide solid solution with multiple components using elemental powder. *Adv Powder Technol* 2020, **31**: 505–509.
[27] Coutures JP, Coutures J. The system HfO_2–TiO_2. *J Am Ceram Soc* 1987, **70**: 383–387.
[28] Noguchi T, Mizuno M. Phase changes in the ZrO_2–TiO_2 system. *Bull Chem Soc Jpn* 1968, **41**: 2895–2899.
[29] Parthasarathy TA, Rapp RA, Opeka M, *et al*. A model for the oxidation of ZrB_2, HfB_2 and TiB_2. *Acta Mater* 2007, **55**: 5999–6010.
[30] Parthasarathy TA, Rapp RA, Opeka M, *et al*. Modeling oxidation kinetics of SiC-containing refractory diborides. *J Am Ceram Soc* 2012, **95**: 338–349.
[31] Kai W, Li CC, Cheng FP, *et al*. The oxidation behavior of an equimolar FeCoNiCrMn high-entropy alloy at 950 ℃ in various oxygen-containing atmospheres. *Corros Sci* 2016, **108**: 209–214.
[32] Zou J, Rubio V, Binner J. Thermoablative resistance of ZrB_2–SiC–WC ceramics at 2400 ℃. *Acta Mater* 2017, **133**: 293–302.
[33] Kiyono H, Shimada S, Sugawara K, *et al*. TEM observation of oxide scale formed on TiC single crystals with different faces. *Solid State Ion* 2003, **160**: 373–380.
[34] Opeka MM, Talmy IG, Zaykoski JA. Oxidation-based materials selection for 2000 ℃+ hypersonic aerosurfaces: Theoretical considerations and historical experience. *J Mater Sci* 2004, **39**: 5887–5904.
[35] Luo L, Wang YG, Duan LY, *et al*. Ablation behavior of C/SiC–HfC composites in the plasma wind tunnel. *J Eur Ceram Soc* 2016, **36**: 3801–3807.
[36] Zeng Y, Xiong X, Li GD, *et al*. Microstructure and ablation behavior of carbon/carbon composites infiltrated with Zr–Ti. *Carbon* 2013, **54**: 300–309.
[37] Luo L, Wang YG, Liu LP, *et al*. Ablation behavior of C/SiC composites in plasma wind tunnel. *Carbon* 2016, **103**: 73–83.
[38] Luo L, Wang YG, Liu LP, *et al*. Carbon fiber reinforced silicon carbide composite-based sharp leading edges in high enthalpy plasma flows. *Compos B Eng* 2018, **135**: 35–42.
[39] McCormack SJ, Tseng KP, Weber RJ, *et al*. *In-situ* determination of the HfO_2–Ta_2O_5-temperature phase diagram up to 3000 ℃. *J Am Ceram Soc* 2019, **102**: 4848–4861.
[40] Magunov RL, Sotulo VS, Magunov IR. Phase relationships in $ZrO_2(HfO_2)$–Nb_2O_5 systems. *Russ J Inorg Chem* 1993, **38**: 341–343.
[41] Wang DN, Zeng Y, Xiong X, *et al*. Ablation behavior of ZrB_2–SiC protective coating for carbon/carbon composites. *Ceram Int* 2015, **41**: 7677–7686.
[42] Bronson A, Chessa J. An evaluation of vaporizing rates of SiO_2 and TiO_2 as protective coatings for ultrahigh temperature ceramic composites. *J Am Ceram Soc* 2008, **91**: 1448–1452.
[43] Opila EJ, Hann RE. Paralinear oxidation of CVD SiC in water vapor. *J Am Ceram Soc* 1997, **80**: 197–205.
[44] Kubikova B, Cibulkova J, Danek V, *et al*. Physicochemical properties of molten KF–K_2NbF_7–Nb_2O_5 system. *ECS Trans* 2007, **3**: 169–178.
[45] Cibulková J, Chrenková M, Vasiljev R, *et al*. Density and viscosity of the $(LiF+NaF+KF)_{eut}$ (1) + K_2TaF_7 (2) + Ta_2O_5 (3) melts. *J Chem Eng Data* 2006, **51**: 984–987.
[46] Nazaré S, Ondracek G, Schulz B. Properties of light water reactor core melts. *Nucl Technol* 1977, **32**: 239–246.
[47] Kim Y, Park H. Estimation of TiO_2–FeO–Na_2O slag viscosity through molecular dynamics simulations for an energy efficient ilmenite smelting process. *Sci Rep* 2019, **9**: 17338.